

Hot Deformation Characteristics of 13Cr-4Ni Stainless Steel Using Constitutive Equation and Processing Map

Brij Kishor, G.P. Chaudhari, and S.K. Nath

(Submitted January 1, 2016; in revised form April 7, 2016; published online June 8, 2016)

Hot compression tests were performed to study the hot deformation characteristics of 13Cr-4Ni stainless steel. The tests were performed in the strain rate range of $0.001\text{--}10\text{ s}^{-1}$ and temperature range of $900\text{--}1100\text{ }^{\circ}\text{C}$ using Gleeble® 3800 simulator. A constitutive equation of Arrhenius type was established based on the experimental data to calculate the different material constants, and average value of apparent activation energy was found to be 444 kJ/mol . Zener-Hollomon parameter, Z , was estimated in order to characterize the flow stress behavior. Power dissipation and instability maps developed on the basis of dynamic materials model for true strain of 0.5 show optimum hot working conditions corresponding to peak efficiency range of about 28–32%. These lie in the temperature range of $950\text{--}1025\text{ }^{\circ}\text{C}$ and corresponding strain rate range of $0.001\text{--}0.01\text{ s}^{-1}$ and in the temperature range of $1050\text{--}1100\text{ }^{\circ}\text{C}$ and corresponding strain rate range of $0.01\text{--}0.1\text{ s}^{-1}$. The flow characteristics in these conditions show dynamic recrystallization behavior. The microstructures are correlated to the different stability domains indicated in the processing map.

Keywords constitutive equation, dynamic recrystallization, flow curve, hot deformation

1. Introduction

The hydro turbine components are used underwater due to which these are affected by the high-speed movement of slurry and pressure. Mostly, hydro turbine blades and runner body are made from the 13% chromium-4% nickel (13Cr-4Ni) martensitic stainless steel (MSS). To improve the erosion resistance of this steel, various techniques and methods such as thermal spray coatings (Ref 1), hot rolling (Ref 2), heat treatments (Ref 3), friction stir processing (Ref 4), and thermomechanical processing (Ref 5, 6) are applied. These components should have the excellent corrosion resistance and good workability (Ref 7). Difficulties are encountered during hot working due to lack of information regarding the process parameters and the hot deformation behavior of this important engineering steel. Excellent hot workability refers to the plastic deformation at high temperatures without the occurrence of fracture or flow localization (Ref 8). True strain, strain rate, and temperature are required to characterize the flow behavior (Ref 9). Generally, cast products are forged or rolled and heat treated to refine a microstructure (Ref 10). Therefore, hot forging influences the mechanical properties of cast MSS. But limited workability at lower temperatures below $925\text{ }^{\circ}\text{C}$ in MSS hinders the hot forging process (Ref 11). Hot deformation contributes to improvement in mechanical properties through microstructural refinement (Ref 12, 13). During deformation, microstructural defects may be produced due to the inhomogeneous effect of temperature and strain rate and result in unsafe domains.

However, homogeneous deformation can produce microstructures free from defects (Ref 14, 15). The improved mechanical properties, i.e., ductility and toughness of 13Cr-4Ni MSS obtained through hot deformation can provide better resistance against the erosion (Ref 4–6). Therefore, the high-temperature flow behavior of 13Cr-4Ni MSS must be studied in order to find out the desired hot working parameters.

In this regard, some workers studied the hot deformation behavior of MSS using constitutive equations and processing maps. Xiao and Guo (Ref 7) performed isothermal compression of 1Cr12Ni3Mo2VNbN MSS in the temperature range of $1253\text{--}1453\text{ K}$ and strain rate range of $0.01\text{--}10\text{ s}^{-1}$. Constitutive equations were found to be a better tool to reveal the effects of true strain, strain rate, and temperature on the flow stress. Momeni et al. (Ref 16) discussed the characteristics of flow curve for 410 MSS and validated through modeling the constitutive equations. Momeni and Dehghani (Ref 17) characterized the hot deformation behavior of AISI 410 MSS in the temperature range of $900\text{--}1150\text{ }^{\circ}\text{C}$ and strain rate range of $0.001\text{--}10\text{ s}^{-1}$ and established constitutive equations and processing maps. Dependence of Zener-Hollomon parameter (Z) on flow stress was analyzed. Hot deformation in the temperature range of $1000\text{--}1125\text{ }^{\circ}\text{C}$ and strain rate range of $0.001\text{--}10\text{ s}^{-1}$ was found to be satisfactory. Most of the investigations regarding hot deformation characterization involve the constitutive equations and processing maps especially for austenitic stainless steels that are validated for actual industrial process such as hot forging. Venugopal et al. (Ref 18) evaluated the hot deformation characteristics of AISI 304L, 316L, and 304 grades of austenitic stainless steels to establish processing, microstructure and property relationships. Sivaprasad et al. (Ref 19) discussed the development of various models for microstructural control during processing for a 15Cr-15Ni Ti-modified austenitic stainless steel. Marchattiwari et al. (Ref 20) investigated the kinetics of dynamic recrystallization (DRX) during hot deformation of 304 austenitic stainless steel based on the characteristics of flow curves. Murty et al. (Ref 21) identified the flow instabilities in the processing maps of AISI 304 stainless steel. Tan et al. (Ref 22) described the processing

Brij Kishor, G.P. Chaudhari and S.K. Nath, Department of Metallurgical and Materials Engineering, Indian Institute of Technology, Roorkee 247667, India. Contact e-mail: chaudhmt@iit.ernet.in.

map and hot workability of Super 304H austenitic heat-resistant stainless steel.

The hot deformation characteristics of 13Cr-4Ni MSS are not studied until now. This is required in order to identify the best processing conditions and for modifying the microstructure because high-temperature deformation of MSS is shown to be a promising technique to refine the microstructure (Ref 23). Therefore, the present work studied the hot deformation characteristics of 13Cr-4Ni MSS by performing compression tests using Gleeble® 3800. The tests were performed in the temperature range of 900-1100 °C and strain rate range of 0.001-10 s⁻¹, for 50% total deformation (true strain of 0.69). Flow stress data obtained from experimental true stress-true strain curves are used to derive the constitutive equations. Material constants and apparent activation energy (*Q*) are determined for true strain range of 0.1-0.69. Flow stress and the values of *Z* parameter are established for the entire range of deformation conditions at true strain of 0.5. Processing map is constructed by superimposition of power dissipation efficiency and instability maps using a true strain of 0.5 based on dynamic materials model (DMM) which follows the continuum criteria (Ref 24, 25). Optical microstructures of deformed specimens corresponding to different regions of processing map are studied in order to characterize the DRX occurred in the stable regions and the instability behavior.

2. Experimental Procedure

The ingot of 13Cr-4Ni MSS obtained from M/s Vaishnav Steel Pvt. Ltd., Muzaffarnagar India, was machined to manufacture 10-mm-diameter and 15-mm-long cylindrical specimens according to the ASTM Standard E209 (Ref 26). The chemical composition of 13Cr-4Ni MSS was determined using Thermo Jarrell Ash spark emission spectroscope and is given in Table 1. *K*-type thermocouple was spot welded on the center of specimen along its length to monitor the true temperature during the deformation. Inside the hot compression chamber, graphite lubricant with 0.05-mm-thick tantalum foil was positioned between the ISO-T anvil and the specimen to reduce the friction and sticking between them. The scheme of deformation is shown in Fig. 1.

All the specimens were heated up to the austenitization temperature of 1100 °C at heating rate of 5 °C/s and soaked for 120 s to homogenize. To attain the deformation temperatures, specimens were cooled down at the rate of 1 °C/s. At deformation temperatures (900, 950, 1000, 1050, and 1100 °C), soaking time of 30 s was allowed to eliminate the thermal gradients. Temperature range of 900-1100 °C is selected in the present study for the following reasons. During the hot deformation, the control of austenite recovery and recrystallization can induce grain refinement (Ref 27). The temperature range of 900-1100 °C covers the range of stability of single-phase austenite for this steel. Delta ferrite forms above 1095 °C which leads to cracking during hot working in martensitic stainless steel grades (Ref 11). Therefore, 1100 °C

was taken as upper limit. Further, in this grade of 13Cr4Ni martensitic stainless steel, carbides are completely dissolved as temperature is increased to 900 °C (Ref 6) and the single-phase austenite remains, which is likely to exhibit good workability. In the scientific literature involving other martensitic stainless steel grades, temperature ranges of 980-1180 °C (Ref 7), 900-1150 °C (Ref 16, 17, 28), and 950-1100 °C (Ref 23) have been employed.

The deformed specimens were compressed by 50% and immediately air quenched. In order to study the microstructural evolution, deformed specimens were cut parallel to the compression axis and internal cut surfaces were polished. Electro-etching using 60% nitric acid + 40% water solution revealed the microstructure using a Leica DMI 5000M light optical microscope. Activation energy, *Q*, is derived from the true stress-true strain data for true strain range of 0.1-0.69. Material constants and *Z* parameter for flow stress are described for true strain of 0.5. Flow stress data are used to construct the processing map.

3. Results

3.1 True Stress-True Strain Curve Behavior

Figure 2 shows the true stress-true strain flow curves of 13Cr-4Ni MSS for various deformation conditions. For deformation conditions at temperatures of (900-1100 °C) and strain rates of 1 and 10 s⁻¹, flow stress increases with strain to a peak followed by continuous softening and thereupon the flow stress reaches a constant value. Flow stresses seem to increase rapidly in the initial stage of deformation followed by a gradual increase. Specimens deformed with 0.1 s⁻¹ at temperatures of 900 and 950 °C also show similar behavior. In the strain rate range of 0.1-0.001 s⁻¹, after reaching the peak, the flow stress decreases up to certain level and follows a steady state (except at 900 and 950 °C) (Fig. 2a-e). Zhou et al. (Ref 29) observed a

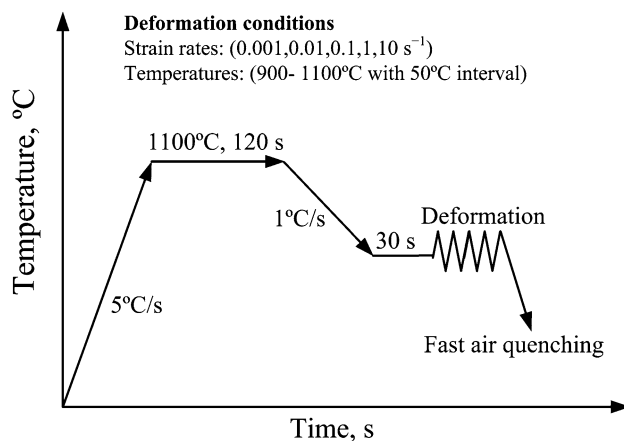


Fig. 1 Schematic diagram for deformation of 13Cr-4Ni MSS

Table 1 Chemical composition (wt.%) of 13Cr-4Ni MSS

C	Si	Mn	P	S	Cr	Ni	Mo	Cu	V	Al	Fe
0.065	0.62	0.73	0.027	0.008	12.30	3.78	0.45	0.22	0.04	0.005	Bal.

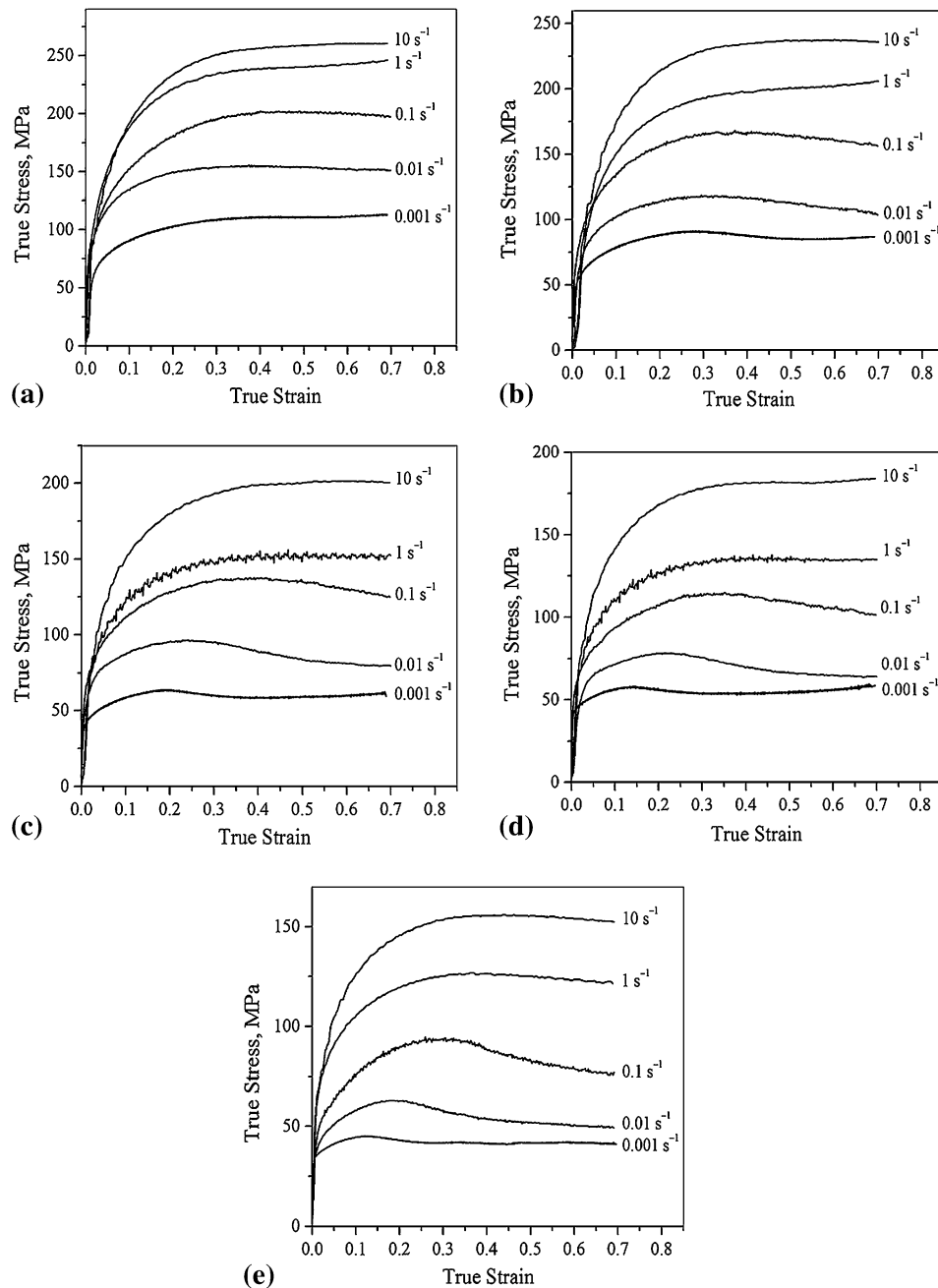


Fig. 2 True stress-true strain curves for 13Cr-4Ni MSS at strain rates from 0.001 to 10 s^{-1} at particular temperatures of (a) 900 °C, (b) 950 °C, (c) 1000 °C, (d) 1050 °C, (e) 1100 °C

similar behavior and defined the dynamic recovery (DRV) and DRX deformation mechanisms according to flow stress response with true strain. In DRV, the flow stress increases up to a peak followed by a constant value with increasing true strain. However, in DRX, the flow stress decreases after reaching a peak, and maintains a steady state. Hence, peak position of flow stress with true strain gives the indication of change in deformation mechanism (Ref 29). For hot compression at 900 and 950 °C at higher strain rates, the flow stress keeps on increasing because the microstructure restoration mechanisms are inhibited due to paucity of time and lower temperature which suppress the diffusional processes.

The plots of peak stress and strain with various strain rates are shown in Fig. 3. Peak stress is found to be higher for lower

deformation temperatures (Fig. 3a). At deformation temperatures of 1000, 1050, and 1100 °C, peak strain increases with the increasing strain rates (Fig. 3b). However, for 900 °C, the peak strain is high at 0.001 s^{-1} , and it drops at 0.01 s^{-1} and follows the increasing trend up to 1 s^{-1} . Subsequently, it drops again. For 950 °C, the peak strain increases from 0.001 to 1 s^{-1} and it drops for 10 s^{-1} . Generally, the peak strain is considered as the initiation point for the commencement of a restoration mechanism and its value increases with strain rate (Ref 30). However, in the present work for lower temperatures of 900 and 950 °C, the variation of peak strain values with true strain showed abnormal manners, suggesting a change in restoration mechanism from continuous DRX (CDRX) to discontinuous DRX (DDRX) (Ref 31).

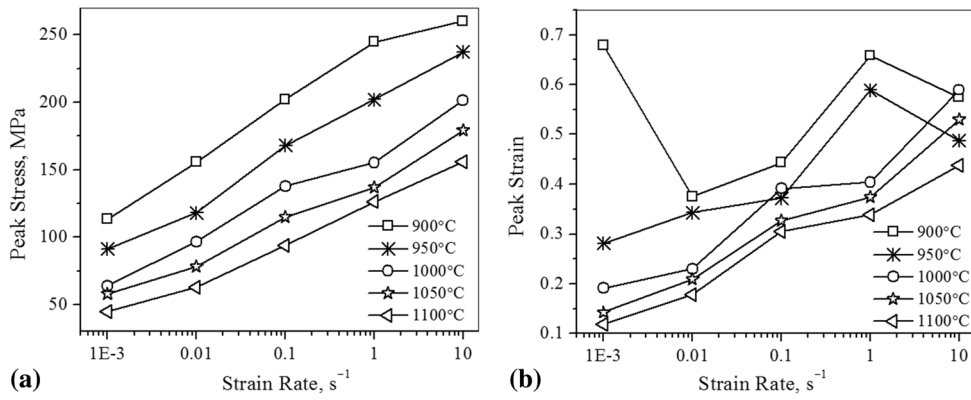


Fig. 3 Plots showing dependence of (a) peak stress and (b) peak strain, on strain rates for different temperatures for processing of 13Cr-4Ni MSS

3.2 Constitutive Equation and Determination of Material Constants

Sellars and Tegart (Ref 32) applied Arrhenius-type equations to correlate the flow stress and strain rate at high deformation temperatures. The mutual effects of different strain rates and temperatures on deformation are expressed by the Z parameter in an exponent-type equation (Ref 33) and this is given as

$$Z = \dot{\epsilon} \exp\left(\frac{Q}{RT}\right) = f(\sigma), \quad (\text{Eq 1})$$

where

$$f(\sigma) = \begin{cases} A\sigma^{n'} & \text{preferred for low } \sigma \text{ level} \\ B \exp(\beta\sigma) & \text{preferred for high } \sigma \text{ level} \\ C[\sinh(\alpha\sigma)]^n & \text{wide range of range of } T \text{ and } \dot{\epsilon} \end{cases} \quad (\text{Eq 2})$$

where σ is the true stress, $\dot{\epsilon}$ is the strain rate, R is the gas constant (8.314 J/mol/K), and T is the temperature in Kelvin. A , B , C , n' , n , β , and $(\alpha = \beta/n)$ are material constants.

The following expressions were derived for fixed deformation temperature and strain conditions:

$$n' = \left[\frac{\partial \ln \dot{\epsilon}}{\partial \ln \sigma} \right]_T \quad (\text{Eq 3})$$

$$\beta = \left[\frac{\partial \ln \dot{\epsilon}}{\partial \sigma} \right]_T \quad (\text{Eq 4})$$

$$n = \left[\frac{\partial \ln \dot{\epsilon}}{\partial \ln[\sinh(\alpha\sigma)]} \right]_T \quad (\text{Eq 5})$$

In the present investigation, the values of flow stress and strain rates are found from the true stress-true strain curves obtained from the experimental hot compression tests for a fixed true strain of 0.5. These values are substituted in to Eq 3, 4, and 5 for temperature range of 900-1100 °C and strain rate range of 0.001-10 s⁻¹. The values of materials constants are obtained by linear fitting of the experimental data through regression analysis. Accordingly, average slopes of the lines shown in Fig. 4(a) and (b) give the respective values of $\beta = 0.065$ and $n' = 7.94$. The stress multiplier α (Ref 28) is measured as $(\alpha = \frac{\beta}{n'} = 0.0082 \text{ MPa}^{-1})$. Value of n is calculated as 5.84 (Fig. 4c). Now, the following relation for a constant strain rate gives the value of Q :

$$Q = nR \left[\frac{\partial \ln[\sinh(\alpha\sigma)]}{\partial (1/T)} \right]_{\dot{\epsilon}} \quad (\text{Eq 6})$$

Similarly, the average slope of all the plots in Fig. 4(d) is 9.04. Activation energy Q is calculated by multiplying this average slope value with nR as given in the relation of Eq 6. The value of Q thus calculated is 439 kJ/mol for 13Cr-4Ni MSS at a true strain of 0.5.

This procedure is repeated for true strains ranging from 0.1 to 0.69 and the corresponding values of α and n are shown in Table 2. The corresponding values of Q with true strain are plotted in Fig. 5(a) and the apparent activation energy (average value) is found to be 444 kJ/mol⁻¹. A higher value of Q is obtained at the lower and higher values of true strain. In general, a higher value of Q is obtained in the beginning of the deformation due to higher energy imposed on specimen to initiate the plastic deformation. It decreased up to a true strain of 0.3 and showed small variation until a true strain of 0.5 is reached. The reason for decrease in the value of Q is the initiation of softening due to DRV and further by DRX. Dehghani et al. (Ref 31) reported that the value of Q increases with strain because the movement of high-angle boundaries during DDRX or low-angle boundaries during CDRX require a higher activation energy than the DRV. Therefore, at strain of 0.6 and 0.69 the value of Q again increases. The values of Q are used to determine the value of Z for all deformation conditions by substituting the values of respective T , R , and strain rates in Eq 1. It is found that the value of $\ln Z$ increases with decrease of temperature and increase of strain rate. These values are plotted for hyperbolic sine function (Fig. 5b) for true strains ranging from 0.1 to 0.69. To determine the value of constant C , the following relation is derived:

$$\ln Z = \ln C + n \ln[\sinh(\alpha\sigma)]. \quad (\text{Eq 7})$$

Average values of intercept of the lines obtained from the plot (Fig. 5b) yield the value of $\ln C$ as 38.01. The value for C is calculated as 3.22×10^{16} . The sinh function for the 13Cr-4Ni MSS is derived by substituting the values of materials constants n , C , and α , into Eq 1 and 2. The constitutive equation obtained is given by

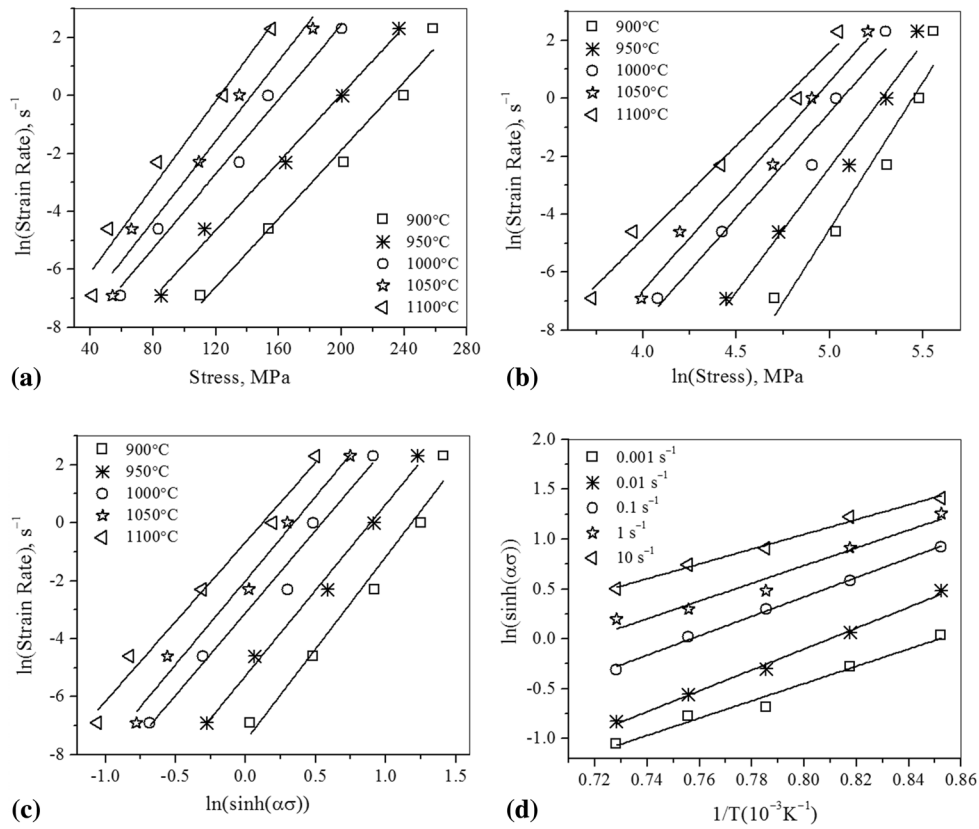


Fig. 4 13Cr-4Ni MSS Plot of $\ln \dot{\epsilon}$ vs. (a) σ , (b) $\ln \sigma$, (c) $\ln(\sinh(\alpha\sigma))$, and $\ln(\sinh(\alpha\sigma))$ vs. (d) $1000/T$ for fixed true strain of 0.5

Table 2 Values of material constants calculated from constitutive equations for 13Cr-4Ni MSS

True strain	α	n
0.1	0.0099	7.57
0.2	0.0086	6.73
0.3	0.0083	6.20
0.4	0.0082	5.96
0.5	0.0082	5.84
0.6	0.0082	5.83
0.69	0.0081	5.88

$$Z = \dot{\epsilon} \exp\left(\frac{439000}{8.314T}\right) = 3.22 \times 10^{16} [\sinh(0.0082\sigma_p)]^{5.84}. \quad (\text{Eq 8})$$

3.3 Processing Map

In the initial stage of deformation, more amount of energy is stored in the material and the rate of power dissipation increases with increase in temperature and strain rate. The rate of power dissipation is represented by a dimensionless parameter (Ref 25) called efficiency of power dissipation (η) and is given as

$$\eta = \frac{2m}{m+1}, \quad (\text{Eq 9})$$

where m is the strain rate sensitivity parameter. Value of m depends on the rate of loading and is calculated as

$$m = \frac{\partial(\ln \sigma)}{\partial(\ln \dot{\epsilon})}. \quad (\text{Eq 10})$$

Stable region during hot deformation corresponds to values of m between 0 and 1. Negative values of m indicate instability in a material. Ziegler (Ref 34) proposed another dimensionless parameter for microstructure instability:

$$\xi(\dot{\epsilon}) = \frac{\partial \ln\left(\frac{m}{m+1}\right)}{\partial \ln \dot{\epsilon}} + m. \quad (\text{Eq 11})$$

Unstable flow is predicted when $\xi(\dot{\epsilon}) < 0$.

In this study, the variation of m in the frame of temperature and $\log \dot{\epsilon}$ is studied for 13Cr-4Ni MSS and is shown in Fig. 6(a) and (b) for a true strain of 0.2 and 0.5, respectively. Figure 6(a) shows that at low strain of 0.2, the low values of m occupy more frame area as compared to the map shown in Fig. 6(b). Values of m tend to decrease and are shifted toward high strain rate and low temperature, which indicate a larger region of instability. Higher positive value of m close to 1 represents excellent hot workability of material (Ref 17).

The contour maps for η are shown in Fig. 7 at true strains of 0.1, 0.2, 0.3, 0.5, and 0.6. True strain of 0.1 and 0.2 correspond to strain close to peak stress. Strain of 0.3 represents the situation for flow softening state and both 0.5 and 0.6 correspond to the steady state. The power dissipation efficiency represents the rate of change of microstructure during the hot deformation (Ref 35), and maximization of η and m reduces the tendency for flow localization (Ref 21). Because the features of maps are similar (Fig. 7a-d), it can be said that the influence of

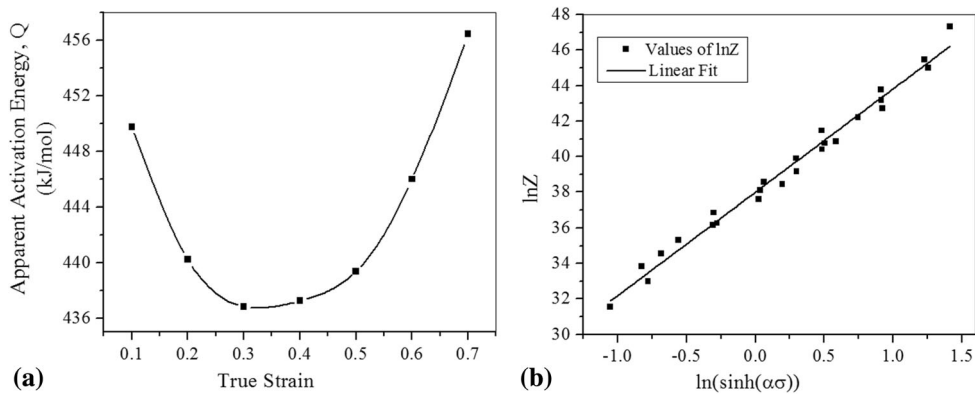


Fig. 5 13Cr-4Ni MSS Plots for (a) Variation of Q vs. true strain and (b) Dependence of flow stress on Z for hyperbolic sine function at true strain of 0.5

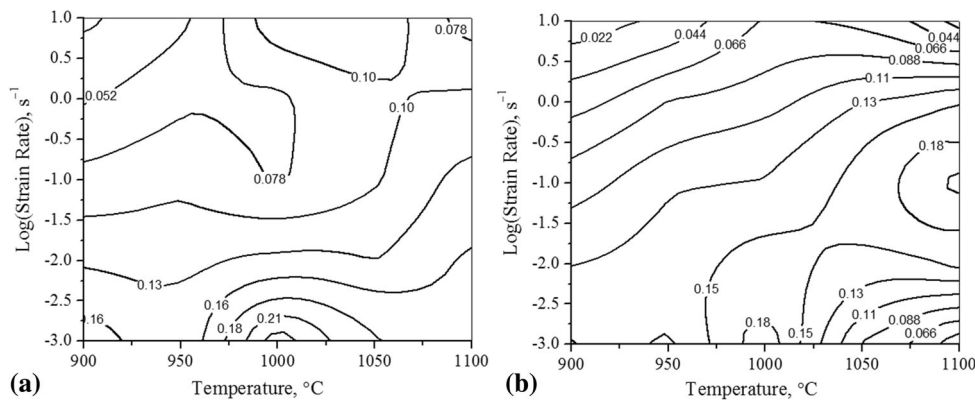


Fig. 6 Contour map of the m -values for 13Cr-4Ni MSS in the frame of deformation temperature and strain rate at true strain of (a) 0.2 and (b) 0.5

true strain on maps is negligible. The values of η increase slightly as the strain increases and show highest values in map developed at 0.3 due to operation of flow softening mechanism. Thus, in this work, the peak value of efficiency is approximately 40%. Power dissipation map developed at strain of 0.5 shows two different domains with peak efficiency range of about 28-32%. First domain lies in the temperature range of 950-1025 °C and strain rate range of 0.001-0.01 s⁻¹; with peak efficiency of about 28% obtained at 1000 °C and 0.001 s⁻¹. Second domain exists in the temperature range of 1050-1100 °C and strain rate range of 0.01-0.1 s⁻¹; showing peak efficiency of about 32% at strain rate of 0.1 s⁻¹ for 1100 °C and 28% for 1050 °C. The stable regions corresponding to higher values of η are expansive. Generally, values of η corresponding to DRX are approximately 30-50% (Ref 17). Flow stress behavior in these regions shows the characteristics of DRX (Fig. 2b-d) and represent the optimum hot working conditions for this steel.

Processing map is obtained by superimposition of instability map over the power dissipation map in the frame of $\log \dot{\epsilon}$ and temperature. The region of flow instability as predicted by continuum criteria given in Eq 11 is delineated by shaded region shown in Fig. 8. Processing map shows instability at high strain rates and at higher temperatures. The values of efficiency in this region are lower as compared to the un-shaded

regions (stable regions), suggesting that most of the power dissipation was converted into heat and evolved in the form of temperature rise (Ref 36). Pan et al. (Ref 37) also reported that a higher processing temperature caused heating and a higher strain rate promotes flow localization due to insufficient time for deformation. A large instability region is observed in the temperature range of 900-1100 °C and in the strain rate range of 1-10 s⁻¹ and a smaller one is observed for the temperature range of 900-920 °C and strain range of 0.001-0.005 s⁻¹. These conditions are detrimental to the hot deformation processing.

4. Discussion

From Fig. 2, the presence of peaks followed by steady-state flow is a good indication for existence of DRX (Ref 28). Momeni and Dehghani (Ref 17) also found this behavior at higher temperatures and low strain rates and reported that a higher work hardening rate slows down the rate of work softening due to DRX. Momeni et al. (Ref 16) achieved the steady-state region in 410 grade MSS at high-temperature and low-strain rate conditions. Thus, in this work, the DRX occurs at higher temperature and low-strain rate conditions because

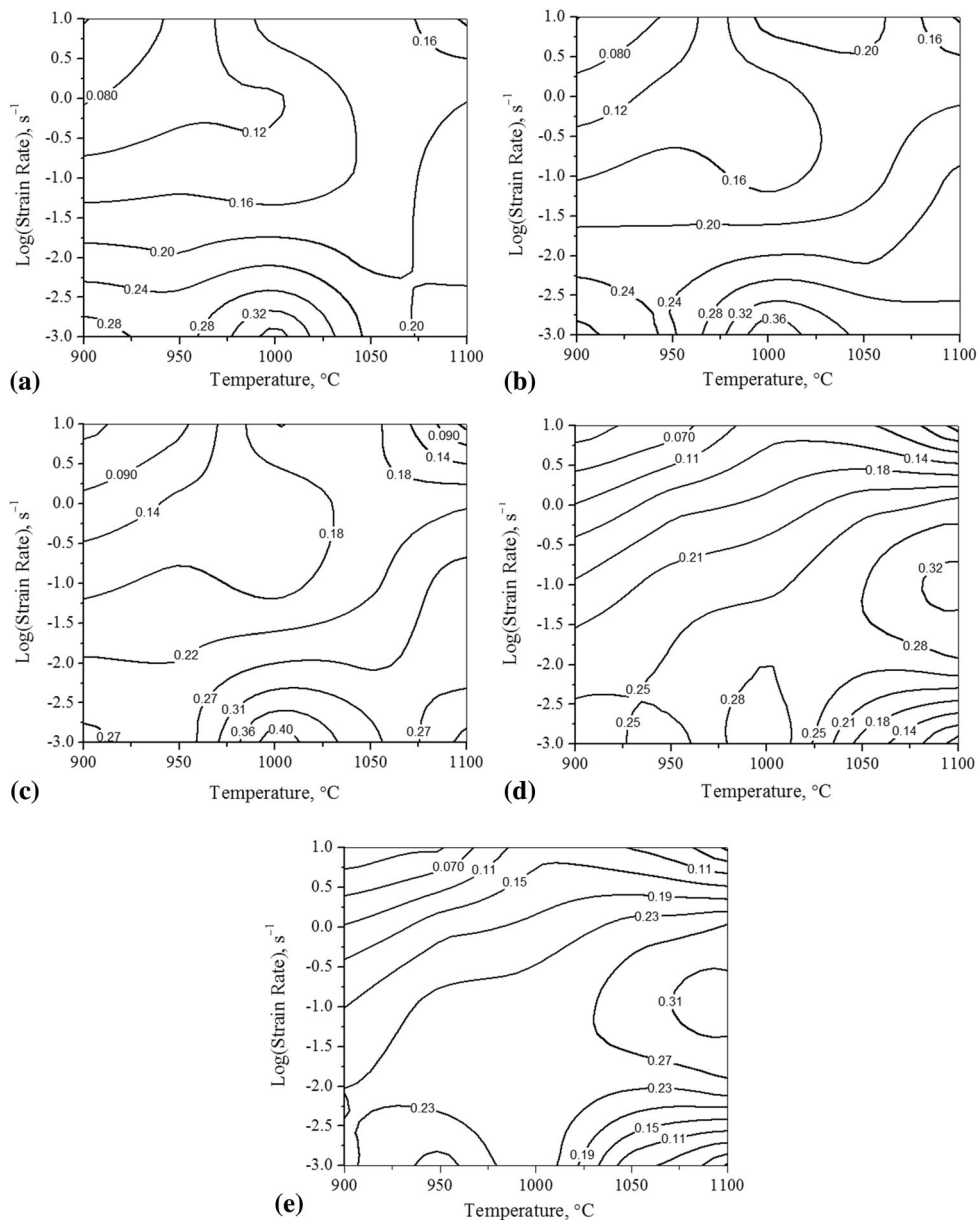


Fig. 7 Power dissipation efficiency contours of 13Cr-4Ni MSS for true strain of (a) 0.1, (b) 0.2, (c) 0.3, (d) 0.5, and (e) 0.6

higher temperature offers higher mobility to the grain boundary and lower strain rate provides longer time for the dislocation annihilation, nucleation of new grains, and growth (Ref 38).

For higher strain rates, specimens show higher work hardening characteristics without a peak or with a single small peak. Work hardening characteristics are observed at 10 s^{-1} due to the insufficient time for nucleation and growth of DRX grains. The heat generated from deformation results in temperature rise that leads to flow softening (Ref 8). It is explained in an earlier study (Ref 39) that there is a slow flow softening stage with increasing strain rate, followed by steady flow at larger strains. Generally, DRX occurs at low strain rates and high temperature, because the critical dislocation density or critical strain for the occurrence of DRX decreases (Ref 40). The change in flow behavior with the deformation is clearly observed in Fig. 3, which shows the variation of the peak strain and peak stress with strain rates for different deformation

temperatures. Dehghani et al. (Ref 31) reported that the peak strain is beneficial to find the actual commencement point for DRX.

On the basis of experimental data and constitutive equation, the materials constants are determined, which show the change in mechanism of hot deformation. At initial deformation, n and α show the higher values and correspondingly the value of Q is also high (Table 2; Fig. 5a). The values of Q show anomalous behavior because different deformation mechanisms operated during the deformation. The average value of Q is determined as 444 kJ/mol. The values of Q for other stainless steels such as austenitic grades of 304 and 316 are reported as 400 and 460 kJ/mol, respectively (Ref 41, 42). While, for martensitic grades such as AISI 410 and 00Cr13Ni5Mo2 super martensitic stainless steel, the Q values are 448 and 439 kJ/mol, respectively (Ref 17, 43). Thus, the value of activation energy for 13Cr-4Ni MSS in the present study is comparable to that of the

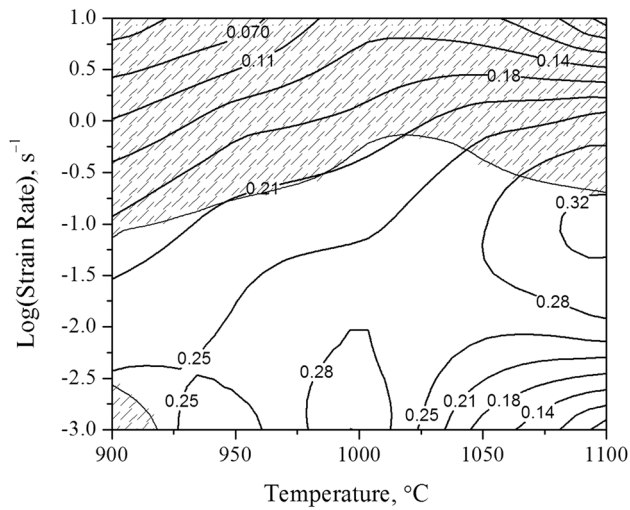


Fig. 8 Processing map of 13Cr-4Ni MSS at a strain of 0.5 using DMM-based model. Shaded regions show instability

other stainless steels. Flow stress behavior is related to the value of Z by a hyperbolic sine function (Fig. 5b). The flow stresses for true strain of 0.5 exhibit linear fit relation with Z parameter, which indicates that the values of Q for all the deformation conditions studied in this work do not vary much (Ref 44).

Processing map based on DMM model is important for optimizing the hot deformation processes and managing the microstructural changes during the forming process (Ref 45). Shi et al. (Ref 10) reported that higher values of η and m are desired for better workability and are associated with the DRX behavior. Lower values of m and η indicate lesser restoration of microstructure. The instability regions are found at higher strain rates, which are primarily manifested as flow localization. It is observed in contour map of Fig. 7 and 8 that the values of η decrease toward the upper left corner, which is due to the occurrence flow localization at high strain rates (Ref 46).

The microstructural features totally change after the hot deformation when compared with as-received (ASR) 13Cr-4Ni MSS specimen (Fig. 9a). All the microstructures exhibit

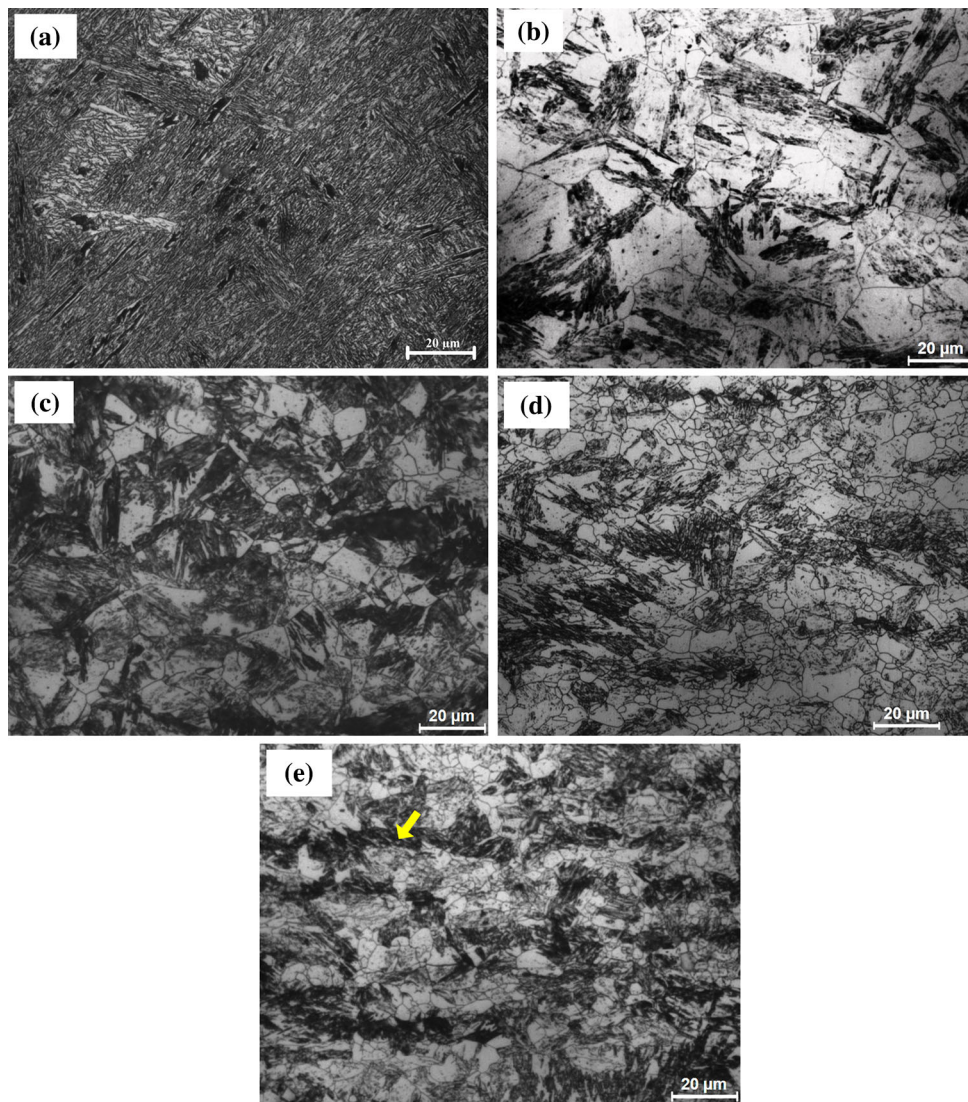


Fig. 9 Optical micrographs of (a) as-received MSS, and hot deformed specimens exhibiting DRX at the deformation conditions of (b) (1000 °C, 0.001 s⁻¹), (c) (1050 °C, 0.1 s⁻¹). Incomplete restoration characteristics are observed for deformation condition of (d) (950 °C, 0.1 s⁻¹). Instability features are observed in (e) (900 °C, 10 s⁻¹) specimen

predominantly martensitic structure for all deformation conditions (Fig. 9). The optical microstructure of ASR 13Cr-4Ni MSS before the deformation is shown in Fig. 9(a). It depicts a fully lath martensite structure. Microstructural evolution during the hot deformation was characterized according to the processing map (Fig. 8) in order to validate the occurrence of DRX, and to confirm the stable and unstable regions. Uniform grain growth and small equiaxed grains along the grain boundaries are observed at the deformation conditions of (1000 °C, 0.001 s⁻¹) and (1050 °C, 0.1 s⁻¹) as shown in Fig. 9(b) and (d). These features demonstrate the occurrence of DRX. The corresponding flow stress characteristics under these conditions also show the DRX behavior (Fig. 2c-d). Thus, these deformation conditions represent optimum hot working domains. For (950 °C, 0.1 s⁻¹) deformation condition, the microstructure revealed partially recrystallized features showing equiaxed grains and remaining recovered structure, showing inhomogeneous distribution of grains (Fig. 9d). It shows the features of incomplete softening mechanism. Microstructure in Fig. 9(e) corresponding to the instability region (900 °C, 10 s⁻¹) revealed localized flow structure and shear bands (see arrow) due to the absence of steady-state behavior (Fig. 2a). It also reveals that the fine grains formed due to recrystallization within the bands. According to processing map, this condition is located in the instability region (Fig. 8). Ebrahimi et al. (Ref 23) explain that as the strain rate increases, stored energy increases from increase in dislocation density which leads to flow instability.

5. Conclusions

The hot deformation characteristics of 13Cr-4Ni MSS are studied in the temperature range of 900-1100 °C and strain rate range of 0.001-10 s⁻¹. Constitutive equations are derived on the basis of true stress-true strain curves and corresponding mechanism for change in microstructures is discussed. The following conclusions are derived from this study:

1. Material constants and values of activation energy for hot deformation of 13Cr-4Ni MSS are determined using the constitutive equations for all deformation conditions in the true strain range of 0.1-0.69. Average value of activation energy is 444 kJ/mol.
2. The Zener-Hollomon parameter is established using the flow stress data at true strain of 0.5, and the following constitutive equation is derived:

$$Z = \dot{\epsilon} \exp\left(\frac{439000}{8.314T}\right) = 3.22 \times 10^{16} [\sinh(0.0082\sigma_p)]^{5.84}$$

3. Power dissipation map developed at strain of 0.5 shows two different domains with peak efficiency in the range of 28-32%. First domain of optimum hot working lies in the temperature range of 950-1025 °C and strain rate range of 0.001-0.01 s⁻¹ with peak efficiency of about 28% obtained at 1000 °C and 0.001 s⁻¹. Second domain occurs in the temperature range of 1050-1100 °C and strain rate range of 0.01-0.1 s⁻¹ showing peak efficiency of about 32% at 1100 °C and 28% at 1050 °C.
4. Microstructural features for the deformation conditions of (1000 °C, 0.001 s⁻¹) and (1050 °C, 0.1 s⁻¹) depict the

DRX behavior while for the deformation conditions of (950 °C, 0.1 s⁻¹) incomplete DRX features are observed. All these conditions lie in the stable region.

5. Two instability domains are obtained, one in the temperature range of 900-1100 °C and strain rate range of 1-10 s⁻¹ and another in the temperature range of 900-920 °C and strain rate range of 0.001-0.005 s⁻¹. Instability regions in the processing map are validated using optical microstructure for the specimen deformed at 900 °C, 10 s⁻¹.

Acknowledgments

The authors are grateful to the Department of Science and Technology, Ministry of Science and Technology, Government of India (Grant Number SR/S3/ME/0029/2009-(G)) for the research funding and FIST grant (Grant number SR/FST/ETI-216/2007) for procuring Gleeble® 3800. M/s. Vaishnav Steel Pvt. Ltd. Muzaffarnagar India is acknowledged for providing the steel.

References

1. J.F. Santa, L.A. Espitia, J.A. Blanco, S.A. Romo, and A. Toro, Slurry and Cavitation Erosion Resistance of Thermal Spray Coatings, *Wear*, 2009, **267**, p 160-167
2. D.C. Wen, Improvement of Slurry Erosion Resistance of Martensitic/Ferritic Duplex Stainless Steel by Hot Rolling, *Met. Mater. Int. J.*, 2010, **16**, p 13-19
3. H.J. Amarendra, P. Kalhan, G.P. Chaudhari, S.K. Nath, and S. Kumar, Slurry Erosion Response of Heat-Treated 13Cr-4Ni Martensitic Stainless Steel, *Mater. Sci. Forum*, 2012, **710**, p 500-505
4. H.S. Grewal, H.S. Arora, H. Singh, and A. Agrawal, Surface Modification of Hydro Turbine Steel Using Friction Stir Processing, *Appl. Surf. Sci.*, 2013, **268**, p 547-555
5. B. Kishor, G.P. Chaudhari, and S.K. Nath, Cavitation Erosion of Thermomechanically Processed 13/4 Martensitic Stainless Steel, *Wear*, 2014, **319**, p 150-159
6. B. Kishor, G.P. Chaudhari, and S.K. Nath, Slurry Erosion of Thermo-Mechanically Processed 13Cr4Ni Stainless Steel, *Tribol. Int.*, 2016, **93**, p 50-57
7. Y.H. Xiao and C. Guo, Constitutive Modelling for High Temperature Behavior of Cr12Ni3Mo2VNbN Martensitic Steel, *Mater. Sci. Eng. A*, 2011, **528**, p 5081-5087
8. S.K. Rajput, M. Dikovits, G.P. Chaudhari, C. Poletti, F. Warchomicka, V. Pancholi, and S.K. Nath, Physical Simulation of Hot Deformation and Microstructural Evolution of AISI, 1016 Steel Using Processing Map, *Mater. Sci. Eng. A*, 2013, **587**, p 291-300
9. S.K. Rajput, G.P. Chaudhari, and S.K. Nath, Physical Simulation of Hot Deformation of Low-Carbon Ti-Nb Microalloyed Steel and Microstructural Studies, *J. Mater. Eng. Perform.*, 2014, **23**, p 2930-2942
10. Z. Shi, X. Yan, and C. Dan, Characterization of Hot Deformation Behaviour of GH925 Super Alloy Using Constitutive Equation, Processing Map And Microstructure Observation, *J. Alloys Compd.*, 2015, **652**, p 30-38
11. G. E. Dieter, H. A. Kuhn, and S. L. Semiatin, Handbook of Workability and Process Design, ISBN: 0-87170-778-0, Materials Park, OH: USA, 2003, p 151-152
12. P. Suikkanen, Development and Processing of Low Carbon Bainitic Steels, Academic Dissertation, Acta Univ. Oul. C 340, Oulun Yliopisto, Oulu, 2009
13. T. Gladman, *The Physical Metallurgy of Microalloyed Steels*, Book 615, The Institute of Materials, London, 1997, p 176-184
14. D. Samantaray, S. Mandal, and A.K. Bhaduri, Optimization of Hot Working Parameters for Thermo-Mechanical Processing of Modified 9Cr-1Mo (P91) Steel Employing Dynamic Materials Model, *Mater. Sci. Eng. A*, 2011, **528**, p 5204-5211

15. S. Venugopal, P. Venugopal, and S.L. Mannan, Optimisation of Cold and Warm Workability of Commercially Pure Titanium Using Dynamic Materials Model (DMM) Instability Maps, *J. Mater. Process. Technol.*, 2008, **202**, p 201–215
16. A. Momeni, K. Dehghani, M. Heidari, and M. Vaseghi, Modeling the Flow Curve of AISI, 410 Martensitic Stainless Steel, *J. Mater. Eng. Perform.*, 2012, **21**, p 2238–2243
17. A. Momeni and K. Dehghani, Characterization of Hot Deformation Behavior of 410 Martensitic Stainless Steel Using Constitutive Equations and Processing Maps, *Mater. Sci. Eng. A*, 2010, **527**, p 5467–5473
18. S. Venugopal and P.V. Sivaprasad, A Journey with Prasad's Processing Maps, *J. Mater. Eng. Perform.*, 2003, **12**, p 674–686
19. P.V. Sivaprasad and S. Venugopal, Instability Maps: An Aid to Tool Design, *J. Mater. Eng. Perform.*, 2003, **12**, p 656–660
20. A. Marchattiwari, A. Sarkar, J.K. Chakravarty, and B.P. Kashyap, Dynamic Recrystallization during Hot Deformation of 304 Austenitic Stainless Steel, *J. Mater. Eng. Perform.*, 2013, **22**, p 2168–2175
21. S.V.S.N. Murty, B.N. Rao, and B.P. Kashyap, Identification of Flow Instabilities in the Processing Maps of AISI, 304 Stainless Steel, *J. Mater. Process. Technol.*, 2005, **166**, p 268–278
22. S. Tan, Z. Wang, S. Cheng, Z. Liu, J. Han, and W. Fu, Processing Maps and Hot Workability of Super304H Austenitic Heat-Resistant Stainless Steel, *Mater. Sci. Eng. A*, 2009, **517**, p 312–315
23. G.R. Ebrahimi, H. Keshmiri, M. Mazinani, A. Maldar, and M. Haghshenas, Multi-Stage Thermomechanical Behaviour of AISI, 410 Martensitic Steel, *Mater. Sci. Eng. A*, 2013, **559**, p 520–527
24. Y.V.R.K. Prasad, H.L. Gegel, S.M. Doraivelu, J.C. Malas, J.T. Morgan, K.A. Lork, and D.R. Barker, Modelling of Dynamic Material Behaviour in Hot Deformation: Forging of Ti-6242, *Metall. Trans. A*, 1984, **15**, p 1883–1892
25. Y.V.R.K. Prasad, Processing Maps: A Status Report, *J. Mater. Eng. Perform.*, 2013, **22**, p 2867–2874
26. ASTM E209, Annual Board of ASTM Standards. ASTM International 3, 2010
27. L. Backe, Modeling the Microstructural Evolution During Hot Deformation of Microalloyed Steels, PhD. Thesis, Royal Institute of Technology Stockholm, 2009
28. F. Ren, J. Chen, and F. Chen, Constitutive Modelling of Hot Deformation Behavior of X20Cr13 Martensitic Stainless Steel with Strain Effect, *Trans. Nonferrous Met. Soc. China*, 2014, **24**, p 1407–1413
29. H. Zhou, Hot Deformation and Processing Maps of As-Extruded Mg-9.8Gd-2.7Y-0.4Zr Mg Alloy, *Mater. Sci. Eng. A*, 2013, **576**, p 101–107
30. A. Momeni, S.M. Abbasi, and H. Badri, Hot Deformation Behavior and Constitutive Modelling of VCN200 Low Alloy Steel, *Appl. Math. Model.*, 2012, **36**, p 5624–5632
31. H. Dehghani, S.M. Abbasi, A. Momeni, and A.K. Taheri, On the Constitutive Modelling and Microstructural Evolution of Hot Compressed A286 Iron-Base Super Alloy, *J. Alloys Compd.*, 2013, **564**, p 13–19
32. C.M. Sellars and W.J. McTegart, On the Mechanism of Hot Deformation, *Acta Metall.*, 1966, **14**, p 1136–1138
33. C. Zener and J.H. Hollomon, Effect of Strain upon Plastic Flow of Steel, *J. Appl. Phys.*, 1944, **15**, p 22–32
34. H. Ziegler, *Progress in Solid Mechanics*, 4th ed., Wiley, New York, 1963, p 93
35. H.G. Sheng, H. Guangojier, W.L. Yun, and P. Fursheng, Processing Map for Hot Working of As Extruded AZ31B Magnesium Alloy, *Trans. Nonferrous Met. Soc. China*, 2005, **15**, p 813–817
36. Y. Ninga, Z. Yaoa, H. Li, H. Guoa, Y. Taob, and Y. Zhang, High Temperature Deformation Behavior of Hot Isostatically Pressed P/M FGH4096 Super Alloy, *Mater. Sci. Eng. A*, 2010, **527**, p 961–966
37. Q.L. Pan, B. Li, Y. Zhang, and Z. Yin, Characterization of Hot Deformation Behavior Of Ni-Base Super Alloy Rene'41 Using Processing Map, *Mater. Sci. Eng. A*, 2013, **585**, p 371–378
38. Y.C. Lin and X.M. Chen, A Critical Review of Experimental Results and Constitutive Descriptions for Metals and Alloys in Hot Working, *Mater. Des.*, 2011, **32**, p 1733–1759
39. C.H. Park, Y.G. Ko, C.S. Lee, K.T. Park, D.H. Shin, and H.S. Lee, High Temperature Deformation Behaviour of ELL, Grade Ti-6Al-4V Alloy with Martensite Microstructure, *Mater. Sci. Forum*, 2007, **551–552**, p 365–372
40. E. Pu, W. Zheng, J. Xiang, Z. Song, and J. Li, Hot Deformation Characteristic and Processing Map of Superaustenitic Stainless Steel S32654, *Mater. Sci. Eng. A*, 2014, **598**, p 174–182
41. A.S. Taylor and P.D. Hodgson, Dynamic Behaviour of 304 Stainless Steel During High Z Deformation, *Mater. Sci. Eng. A*, 2011, **528**, p 3310–3320
42. N.D. Ryan and H.J. McQueen, Hot Strength and Microstructural Evolution of 316 Stainless Steel During Simulated Multistage Deformation by Torsion, *J. Mater. Process. Technol.*, 1993, **36**, p 103–123
43. D. Zou, Y. Han, D. Yan, D. Wang, W. Zhang, and G. Fan, Hot Workability of 00Cr13Ni5Mo2 Supermartensitic Stainless Steel, *Mater. Des.*, 2011, **32**, p 4443–4448
44. A.M.J. Junior, Prediction of Steel Flow Stresses under Hot Working Conditions, *Mater. Res.*, 2005, **3**, p 1980–5373
45. G. Liu, Y. Han, Z. Shi, J. Sun, D. Zou, and G. Qiao, Hot Deformation and Optimization of Process Parameters of an As-Cast 6Mo Superaustenitic Stainless Steel: A Study with Processing Map, *Mater. Des.*, 2014, **53**, p 662–672
46. F. Chen, Z.S. Cui, and D.S. Sui, Recrystallization of 30Cr2Ni4MoV Ultra-Super Critical Rotor Steel during Hot Deformation, Part III: Metadynamic Recrystallization, *Mater. Sci. Eng. A*, 2012, **540**, p 46–54